# UNCONDITIONALLY ENERGY STABLE SCHEMES FOR THE INEXTENSIBLE INTERFACE PROBLEM WITH BENDING[*]

MING-CHIH LAI[†] AND KIAN CHUAN ONG[‡]

**Abstract.** In this paper, we develop unconditionally energy stable schemes to solve the inextensible interface problem with bending. The fundamental problem is formulated by the immersed boundary method where the nonstationary Stokes equations are considered, with the elastic tension and bending forces expressed in terms of Dirac delta function along the interface. The elastic tension is one of the solution variables which plays the role of Lagrange multiplier to enforce the inextensibility of the interface. Both the backward Euler and Crank–Nicolson methods are introduced and it can be proved that the total energy, i.e., kinetic energy and bending energy, is discretely bounded. The numerical results show that both schemes are unconditionally energy stable without any time-step restriction. The backward Euler scheme is also applied to study the dynamics of vesicles suspended in a shear flow.

**Key words.** immersed boundary method, unconditionally energy stable scheme, inextensible interface, bending

**AMS subject classifications.** 65M06, 76D07

**DOI.** 10.1137/18M1210277

**1. Introduction.** The immersed boundary (IB) method proposed by Peskin [1] has been successfully applied to various fluid-structure interaction problems. A comprehensive review of the IB method is presented in [2]. The IB formulation utilizes an Eulerian frame for the fluid velocity and a Lagrangian frame for the configuration of the immersed elastic structure (immersed boundary or interface). The immersed structure exerts certain forces into the fluid that drive the fluid flow, and at the same time, the fluid flow carries the immersed structure to a new configuration. The fluid-structure interaction between the fluid and the immersed structure is coupled through a force spreading and a velocity interpolating operator by the usage of the smoothed version of the Dirac delta function [2]. The IB formulation is efficient and easy to implement because the immersed structure (regardless of complexity) is regarded as a force generator to the fluid so the fluid variables can be solved in a static Eulerian domain without generating any structure-conforming grid. Therefore, a variety of efficient fluid solvers can be exploited.

Although substantial success has been achieved in the practical applications using the IB method, it still possesses several deficiencies from the numerical point of view. First, the IB method is restricted to first-order accurate even though second-order accurate fluid solvers are used. Since the immersed elastic structure is usually one-dimensional lower than the fluid space, the exerted force is singular (delta function like) and smoothing the delta function in the regular finite difference scheme limits the

[†]Corresponding author. Department of Applied Mathematics, National Chiao Tung University, 1001, Ta Hsueh Road, Hsinchu 300, Taiwan (mclai@math.nctu.edu.tw).

[‡]National Center for Theoretical Sciences, No. 1, Sec. 4, Roosevelt Road, Astronomy-Mathematics Building, National Taiwan University, Taipei 10617, Taiwan (kcong@ncts.ntu.edu.tw).

method to being first-order accurate only. Although several attempts have been made to improve the accuracy, including adaptive local mesh refinements near the immersed boundary, those methods remain formally second-order accurate [3, 4, 5, 6, 7].

Another numerical issue arises from the stability. As revealed in the literature [8, 9, 10, 2], the IB method suffers a stringent time-step restriction to maintain its numerical stability. This restriction becomes severe when the elastic force is stiff, and the force spreading is evaluated at the beginning of each time-step (explicit IB scheme). Such a time-step restriction cannot be elevated effectively even if the fluid solver is discretized in a semi-implicit manner, i.e., explicit differencing of the advection term and implicit differencing of the diffusion term. Rather than performing the force spreading at the beginning of each time-step, one of the remedies is to perform the procedure at each intermediate (semi-implicit IB scheme) stage or at the end of each time-step (implicit IB scheme). However, there is always a trade-off between the stability and the efficiency of those algorithms. The fully implicit IB schemes lead to a nonlinear system of equations which limit the range of applicable solvers, while the semi-implicit IB schemes result in a linear system of equations which provide the possibilities of efficient solvers. In the past decade, there have been many attempts to reduce the stiffness or to overcome the severe time-step restriction in the development of the fully implicit IB scheme and the semi-implicit IB scheme [11, 12, 14, 15, 16, 17, 18]. It was ultimately identified that numerical instability is attributed to a lack of energy conservation [11, 12]. The semi-implicit IB schemes proposed by [11] are proven to be unconditionally stable such that the discrete energy is bounded, considering the discrete force spreading and interpolation operators are discretized at the same location in space and time. Subsequently, within the context of unconditionally stable semi-implicit IB schemes, several efficient algorithms and linear solvers are explored. For instance, approximate projection methods [11], the double Schur complement [12], the geometric multigrid method [18], and the projection method with preconditioners [19].

In past decades, the study of the morphological dynamics of biological cell membranes and vesicles has been an active source of mathematical modeling in biology, biophysics, and bioengineering. The biological system poses challenges to develop efficient and accurate numerical schemes, and the IB method provides a versatile approach to tackle the problem [20, 21, 22, 23, 24, 25, 26]. In the present study, we shall propose new semi-implicit IB schemes for solving the inextensible interface problem with bending that were proven to be unconditionally stable, i.e., bounded discrete energy. The present method and stability analysis differ from the first author's previous work [13] in which the nearly inextensible approach is adopted and no bending effect is considered there. The rest of the paper is organized as follows. In section 2, we introduce the formulation of incompressible Stokes equations with an immersed inextensible interface. Then, we provide the continuous energy estimate in section 3. In section 4, we develop semi-implicit IB schemes based on the backward Euler (BE) and Crank–Nicolson (CN) schemes and show that those developed schemes are unconditionally energy stable. The details of numerical methods are described in section 5, followed by numerical results consisting of energy stability check, grid convergence studies, and an application of vesicle dynamics in section 6. Finally, some conclusions are presented in section 7.

**2. Equations of motion.** We begin by stating the governing equations for an enclosed inextensible interface with bending immersed in a two-dimensional viscous incompressible fluid domain $\Omega$. This model is motivated by the vesicle problem that has attracted significant attention in past years. Throughout this paper, the inextensible

interface is also called the vesicle boundary. Here, we assume that the vesicle and the fluid have the properties of matched density and viscosity. The equations of motion in IB formulation can be written as

$$(2.1) \qquad \rho\frac{\partial \mathbf{u}}{\partial t} + \nabla p = \mu\Delta\mathbf{u} + S(\mathbf{F}_\sigma) + S(\mathbf{F}_b) \quad \text{in } \Omega,$$

$$(2.2) \qquad \nabla \cdot \mathbf{u} = 0 \quad \text{in } \Omega,$$

$$(2.3) \qquad S(\mathbf{F}_\sigma) = \int_\Gamma \frac{\partial}{\partial s}(\sigma\boldsymbol{\tau})\delta(\mathbf{x} - \mathbf{X}(s,t)) \; \mathrm{d}s,$$

$$(2.4) \qquad S(\mathbf{F}_b) = -\int_\Gamma c_b \frac{\partial^4 \mathbf{X}}{\partial s^4}\delta(\mathbf{x} - \mathbf{X}(s,t)) \; \mathrm{d}s,$$

$$(2.5) \qquad \frac{\partial \mathbf{X}}{\partial t}(s,t) = \mathbf{U}(s,t) = \int_\Omega \mathbf{u}(\mathbf{x},t)\delta(\mathbf{x} - \mathbf{X}(s,t))d\mathbf{x} \quad \text{on } \Gamma,$$

$$(2.6) \qquad \nabla_s \cdot \mathbf{U} = \frac{\partial \mathbf{U}}{\partial s} \cdot \boldsymbol{\tau} = 0 \quad \text{on } \Gamma,$$

where $\rho$ is the density, $\mathbf{u}$ the velocity, $p$ the pressure, and $\mu$ the viscosity. Here, the vesicle boundary configuration $\Gamma$ is an enclosed interface represented by Lagrangian markers $\mathbf{X}(s,t)$ with $s$ the arc-length parameter. Since the vesicle is inextensible (2.6), the total arc-length of $\Gamma$ is conserved. The notation $\boldsymbol{\tau}(s,t) = \frac{\partial \mathbf{X}}{\partial s}$ is the unit tangent vector and $c_b$ is the constant bending rigidity. The forces arising from the vesicle boundary $\Gamma$ have two terms, namely, the elastic tension force $\mathbf{F}_\sigma$ in (2.3) and the bending force $\mathbf{F}_b$ in (2.4), which can be derived by taking the variational derivative of Helfrich type energy as shown in [27]. Note that the elastic tension $\sigma(s,t)$ is a self-adjusting unknown function (Lagrange multiplier) to enforce the inextensibility constraint (2.6) which is exactly similar to the role of pressure to enforce the fluid incompressibility (2.2). Certainly, the above governing equations should be accompanied with initial conditions for the velocity and vesicle boundary configuration, and suitable velocity boundary condition on $\partial\Omega$. For simplicity, the periodic boundary condition is employed throughout the study, particularly in the following energy estimates. As far as we know, the solvability of the whole continuous system of (2.1)–(2.6) has not yet been rigorously investigated. Nevertheless, the well-posedness of the steady problem, associated to the system in the absence of bending force (2.4), has been studied recently by Liu, Song, and Xu [28] using weak formulation, and the inf-sup condition has been established successfully. Certainly, the proof of well-posedness of (2.1)–(2.6) is a very important theoretical problem and we shall leave it for future work.

**3. Continuous energy estimate.** We define the inner product of functions on $\Omega$ and $\Gamma$ in the following:

$$(3.1) \qquad \langle \mathbf{u}, \mathbf{v} \rangle_\Omega = \int_\Omega \mathbf{u}(\mathbf{x},t) \cdot \mathbf{v}(\mathbf{x},t) \; \mathrm{d}\mathbf{x}, \quad \langle f,g \rangle_\Gamma = \int_\Gamma f(s,t)\,g(s,t) \; \mathrm{d}s.$$

Thus, the $L^2$ norm of functions on $\Omega$ and $\Gamma$ can be defined as $\|\mathbf{u}\|_\Omega^2 = \langle \mathbf{u}, \mathbf{u} \rangle_\Omega$ and $\|f\|_\Gamma^2 = \langle f,f \rangle_\Gamma$, respectively. Note that the inner product on $\Gamma$ can be extended to the vector-valued functions by $\langle \mathbf{f}, \mathbf{g} \rangle_\Gamma = \int_\Gamma \mathbf{f}(s,t) \cdot \mathbf{g}(s,t) \; \mathrm{d}s$ so that $\|\mathbf{f}\|_\Gamma^2 = \langle \mathbf{f}, \mathbf{f} \rangle_\Gamma$. Taking the inner product of (2.1) by $\mathbf{u}$ and integrating in $\Omega$ yields

$$(3.2) \qquad \rho\left\langle \frac{\partial \mathbf{u}}{\partial t}, \mathbf{u} \right\rangle_\Omega + \langle \nabla p, \mathbf{u} \rangle_\Omega = \langle \mu\Delta\mathbf{u}, \mathbf{u} \rangle_\Omega + \langle S(\mathbf{F}_\sigma) + S(\mathbf{F}_b), \mathbf{u} \rangle_\Omega.$$

Invoking the incompressibility condition (2.2) and periodic boundary condition for the velocity, the above equation can be simplified as

$$(3.3) \qquad \frac{d}{dt}\frac{\rho}{2}\|\mathbf{u}\|_{\Omega}^2 = -\mu\|\nabla\mathbf{u}\|_{\Omega}^2 + \langle S(\mathbf{F}_{\sigma}) + S(\mathbf{F}_b), \mathbf{u}\rangle_{\Omega}.$$

In the IB formulation, the spreading operator acting on the elastic tension force $\mathbf{F}_{\sigma}$ and the surface divergence operator of the velocity are skew-adjoint to each other; see the references in [21, 30]. For completeness, we provide the derivation herein.

The spreading operator acting on the elastic tension force reads

$$\langle S(\mathbf{F}_{\sigma}), \mathbf{u}\rangle_{\Omega} = \int_{\Omega}\left(\int_{\Gamma}\frac{\partial}{\partial s}(\sigma\boldsymbol{\tau})\delta(\mathbf{x} - \mathbf{X}(s,t))\, \mathrm{d}s\right) \cdot \mathbf{u}(\mathbf{x},t)\, \mathrm{d}\mathbf{x}$$

$$= \int_{\Gamma}\frac{\partial}{\partial s}(\sigma\boldsymbol{\tau}) \cdot \left(\int_{\Omega}\mathbf{u}(\mathbf{x},t)\delta(\mathbf{x} - \mathbf{X}(s,t))\, \mathrm{d}\mathbf{x}\right)\, \mathrm{d}s$$

$$= -\int_{\Gamma}\sigma\left(\boldsymbol{\tau} \cdot \frac{\partial\mathbf{U}}{\partial s}\right)\, \mathrm{d}s \quad \text{(applying the integration by parts)}$$

$$(3.4) \qquad = \int_{\Gamma}\sigma\left(-\frac{\partial\mathbf{U}}{\partial s} \cdot \boldsymbol{\tau}\right)\, \mathrm{d}s = \langle\sigma, -\nabla_s \cdot \mathbf{U}\rangle_{\Gamma} = 0 \quad \text{(by (2.6))}.$$

As mentioned, analogous to pressure, the unknown elastic tension $\sigma$ solely acts as a Lagrange multiplier to enforce the inextensibility constraint (2.6) on the vesicle boundary $\Gamma$.

The spreading operator acting on the bending force reads

$$\langle S(\mathbf{F}_b), \mathbf{u}\rangle_{\Omega} = \int_{\Omega}\left(-\int_{\Gamma}c_b\frac{\partial^4\mathbf{X}}{\partial s^4}\delta(\mathbf{x} - \mathbf{X}(s,t))\, \mathrm{d}s\right) \cdot \mathbf{u}(\mathbf{x},t)\, \mathrm{d}\mathbf{x}$$

$$= -\int_{\Gamma}c_b\frac{\partial^4\mathbf{X}}{\partial s^4} \cdot \left(\int_{\Omega}\mathbf{u}(\mathbf{x},t)\delta(\mathbf{x} - \mathbf{X}(s,t))\, \mathrm{d}\mathbf{x}\right)\, \mathrm{d}s$$

$$= -\int_{\Gamma}c_b\frac{\partial^4\mathbf{X}}{\partial s^4} \cdot \mathbf{U}(s,t)\, ds$$

$$= -\int_{\Gamma}c_b\frac{\partial^2\mathbf{X}}{\partial s^2} \cdot \frac{\partial^2\mathbf{U}}{\partial s^2}\, ds \quad \text{(applying integration by parts twice)}$$

$$= -\int_{\Gamma}c_b\frac{\partial^2\mathbf{X}}{\partial s^2} \cdot \frac{\partial^2\mathbf{X}_t}{\partial s^2}\, ds \quad \text{(by (2.5))}$$

$$(3.5) \qquad = -\frac{d}{dt}\int_{\Gamma}\frac{c_b}{2}\frac{\partial^2\mathbf{X}}{\partial s^2} \cdot \frac{\partial^2\mathbf{X}}{\partial s^2} = -\frac{d}{dt}\int_{\Gamma}\frac{c_b}{2}\left|\frac{\partial^2\mathbf{X}}{\partial s^2}\right|^2\, ds.$$

By substituting (3.4)–(3.5) into (3.3), we obtain the following energy estimate:

$$(3.6) \qquad \frac{d}{dt}\left(\frac{\rho}{2}\|\mathbf{u}\|_{\Omega}^2 + \frac{c_b}{2}\left\|\frac{\partial^2\mathbf{X}}{\partial s^2}\right\|_{\Gamma}^2\right) = -\mu\|\nabla\mathbf{u}\|_{\Omega}^2.$$

where the total energy of the system consists of the fluid kinetic energy (the first term) and the vesicle bending energy (the second term).

**4. Numerical discretization.** Now, we are ready to discretize (2.1)–(2.6) by the IB method. For simplicity, we assume a computational rectangular domain $\Omega = [0, L_x] \times [0, L_y]$. The fluid variables are defined on the staggered marker-and-cell

(MAC) grid introduced by Harlow and Welsh [29]; precisely, the pressure is defined at the cell center labeled as $\mathbf{x} = (x_i, y_j) = ((i - 1/2)\Delta x, (j - 1/2)\Delta y)$, $i = 1, 2, \ldots, m$ and $j = 1, 2, \ldots, n$, while the velocity components $u$ and $v$ are defined at cell edges $(x_{i-1/2}, y_j) = ((i - 1)\Delta x, (j - 1/2)\Delta y)$ and $(x_i, y_{j-1/2}) = ((i - 1/2)\Delta x, (j - 1)\Delta y)$, respectively. Here, though it is not necessary, we assume a uniform mesh width $h = \Delta x = \Delta y$. For the immersed vesicle boundary, we use a collection of $M$ discrete points $s_k = k\Delta s, k = 0, 1, \ldots M - 1$, with mesh width $\Delta s$ comparable to the grid mesh $h$. The Lagrangian markers are denoted by $\mathbf{X}_k = \mathbf{X}(s_k)$. Since the vesicle boundary is closed, we define $\mathbf{X}_M = \mathbf{X}_0$. The elastic tension is defined at the "half-integer" point given by $s_{k-1/2} = (k - 1/2)\Delta s$ so we denote it as $\sigma_{k-1/2}$. For any function $\phi(s)$ defined on the immersed interface, we introduce three different approximations to the partial derivative $\frac{\partial \phi}{\partial s}$, namely, the forward, backward, and central difference schemes, as

$$D_s^+ \phi(s) = \frac{\phi(s + \Delta s) - \phi(s)}{\Delta s}, \quad D_s^- \phi(s) = \frac{\phi(s) - \phi(s - \Delta s)}{\Delta s},$$

(4.1)
$$D_s \phi = \frac{\phi(s + \Delta s/2) - \phi(s - \Delta s/2)}{\Delta s}.$$

Thus, the unit tangent can be approximated by $\boldsymbol{\tau} = D_s \mathbf{X}$, which in turn is defined at the "half-integer" points.

Let $\Delta t$ be the time-step size and the superscript index be the time-step level. At the beginning of each time level $n$, the boundary configuration $\mathbf{X}_k^n$, and the unit tangent $\boldsymbol{\tau}_{k-1/2}^n$ are all given. In the present study, our numerical discretization and energy stability analysis are based on the unsteady Stokes equations instead of the Navier–Stokes equations. For the latter case, the nonlinear advection term can be treated explicitly during the time evolution with a moderate CFL condition. Alternatively, the Navier–Stokes equations can be split into an advection part and an unsteady Stokes part in which the advection equation is solved by the alternating direction implicit method to maintain the unconditionally numerical stability [15].

Here we introduce two different time integrations, namely, the BE scheme,

(4.2)   $$\rho \frac{\mathbf{u}^{n+1} - \mathbf{u}^n}{\Delta t} + \nabla_h p^{n+1} = \mu \Delta_h \mathbf{u}^{n+1} + S_h^n(\mathbf{F}_\sigma^{n+1}) + S_h^n(\mathbf{F}_b^{n+1}) \quad \text{in } \Omega_h,$$

(4.3)   $$\nabla_h \cdot \mathbf{u}^{n+1} = 0 \quad \text{in } \Omega_h,$$

(4.4)   $$S_h^n(\mathbf{F}_\sigma^{n+1}) = \sum_{k=1}^M D_s \left(\sigma^{n+1}\boldsymbol{\tau}^n\right)_k \delta_h(\mathbf{x} - \mathbf{X}_k^n)\Delta s,$$

(4.5)   $$S_h^n(\mathbf{F}_b^{n+1}) = -c_b \sum_{k=1}^M D_s^+ D_s^- D_s^+ D_s^- \mathbf{X}_k^{n+1} \delta_h(\mathbf{x} - \mathbf{X}_k^n)\Delta s,$$

(4.6)   $$\mathbf{U}_k^{n+1} = \sum_{\mathbf{x}} \mathbf{u}(\mathbf{x})^{n+1}\delta_h(\mathbf{x} - \mathbf{X}_k^n) h^2 \quad \forall k,$$

(4.7)   $$\nabla_{s_h} \cdot \mathbf{U}_k^{n+1} = D_s^- \mathbf{U}_k^{n+1} \cdot \boldsymbol{\tau}_{k-1/2}^n = 0 \quad \forall k,$$

(4.8)   $$\frac{\mathbf{X}_k^{n+1} - \mathbf{X}_k^n}{\Delta t} = \mathbf{U}_k^{n+1} \quad \forall k,$$

and the CN scheme

(4.9)
$$\rho\frac{\mathbf{u}^{n+1} - \mathbf{u}^n}{\Delta t} + \nabla_h p^{n+1/2} = \frac{\mu}{2}\Delta_h(\mathbf{u}^{n+1} + \mathbf{u}^n) + S_h^{n-1/2}(\mathbf{F}_\sigma^{n+1/2}) + S_h^{n-1/2}(\mathbf{F}_b^{n+1/2}),$$

$$(4.10)\qquad \nabla_h \cdot \mathbf{u}^{n+1} = 0,$$

$$(4.11)\qquad S_h^{n-1/2}(\mathbf{F}_\sigma^{n+1/2}) = \sum_{k=1}^{M} D_s\left(\sigma^{n+1/2}\boldsymbol{\tau}^{n-1/2}\right)_k \delta_h(\mathbf{x} - \mathbf{X}_k^{n-1/2})\Delta s,$$

$$(4.12)\qquad S_h^{n-1/2}(\mathbf{F}_b^{n+1/2}) = -c_b\sum_{k=1}^{M} D_s^+ D_s^- D_s^+ D_s^- \mathbf{X}_k^{n+1/2}\, \delta_h(\mathbf{x} - \mathbf{X}_k^{n-1/2})\Delta s,$$

$$(4.13)\qquad \mathbf{U}_k^{n+1/2} = \sum_{\mathbf{x}} \frac{\mathbf{u}(\mathbf{x})^{n+1} + \mathbf{u}(\mathbf{x})^n}{2}\delta_h(\mathbf{x} - \mathbf{X}_k^{n-1/2})\, h^2 \quad \forall k,$$

$$(4.14)\qquad \nabla_{s_h} \cdot \mathbf{U}_k^{n+1/2} = D_s^- \mathbf{U}_k^{n+1/2} \cdot \boldsymbol{\tau}_{k-1/2}^{n-1/2} = 0 \quad \forall k,$$

$$(4.15)\qquad \frac{\mathbf{X}_k^{n+1} - \mathbf{X}_k^n}{\Delta t} = \mathbf{U}_k^{n+1/2} \quad \forall k.$$

The spatial operators $\nabla_h$ and $\Delta_h$ are the standard second-order central difference approximations to the gradient and Laplacian on the MAC grid. $\delta_h$ is the discrete delta function. Note that $\mathbf{X}_k^{n+1/2}$, $\mathbf{X}_k^{n-1/2}$, and $\boldsymbol{\tau}_{k-1/2}^{n-1/2}$ in the CN scheme are linearly approximated by $\mathbf{X}_k^{n+1/2} = (\mathbf{X}_k^n + \mathbf{X}_k^{n+1})/2$, $\mathbf{X}_k^{n-1/2} = (\mathbf{X}_k^n + \mathbf{X}_k^{n-1})/2$, and $\boldsymbol{\tau}_{k-1/2}^{n-1/2} = (\boldsymbol{\tau}_{k-1/2}^n + \boldsymbol{\tau}_{k-1/2}^{n-1})/2$, respectively. The spreading operator $S_h^{n-1/2}$ used in the CN scheme is for the linearization of $S_h^{n+1/2}$ by lagging one discrete time-step $\Delta t$ for the interface position at time $t = (n - 1/2)\Delta t$ instead of $t = (n + 1/2)\Delta t$. This is exactly like the BE scheme that uses the spreading operator $S_h^n$ for the interface position at $t = n\Delta t$ instead of $t = (n + 1)\Delta t$. To be consistent, the discrete inextensibility constraint in present schemes also uses the one time-step lagging interface tangents, which linearizes the constraint as well. Here, we want to emphasize that the lagged operator is popularly used in IB simulations. Lagging the spreading and interpolation operators results in a linear system of equations which provides a variety of linear solvers applicable to the problem. Not lagging those operators results in a set of nonlinear equations for the implicit system [7]. This time lagging technique might reduce accuracy; however, a predictor-corrector approach which uses the lagged interface position to construct the spreading operator $S$ in the predictor step and the predicted interface to construct the same operator in the corrector step does not exactly recover to full second-order accuracy. (This kind of predictor-corrector approach is called formally second-order accurate, and it is a fully second-order method only when the sharp interface is replaced by an elastic shell with thickness [4, 7, 22].) In fact, it is well known that the IB method is only first-order accurate due to the discretization of the singular delta function force in the formulation [2]. The authors have implemented the predictor-corrector IB method as in [4] for the vesicle in shear flow and the results are not significantly better than the ones shown in Table 3, so we omit them here. Hence, the time lagging technique is crucial for the discretization of the IB problem because it not only yields a linear system for the resultant matrix but also provides flexibility in solving the discretized equations and facilitates the foundation of the present energy stability analysis, as seen below.

**4.1. Energy stability analysis.** In this subsection, we follow the similar energy analysis proposed in [11, 15] and perform the energy stability analysis for our present schemes. We shall show that both methods are unconditionally stable in the sense that total energy is decreasing.

To proceed, we define the kinetic energy $K$ and bending energy $B$ of the system as
(4.16)
$$K = \frac{\rho}{2}\|\mathbf{u}\|_{\Omega_h}^2 = \frac{\rho}{2}\langle\mathbf{u},\mathbf{u}\rangle_{\Omega_h}, \qquad B = \frac{c_b}{2}\|D_s^+ D_s^- \mathbf{X}\|_{\Gamma_h}^2 = \frac{c_b}{2}\langle D_s^+ D_s^- \mathbf{X}, D_s^+ D_s^- \mathbf{X}\rangle_{\Gamma_h},$$

where the associated discrete inner products are defined as

$$(4.17) \qquad \langle\mathbf{u},\mathbf{v}\rangle_{\Omega_h} = \sum_{\mathbf{x}} \mathbf{u}(\mathbf{x})\cdot\mathbf{v}(\mathbf{x})\, h^2, \qquad \langle\phi,\psi\rangle_{\Gamma_h} = \sum_{k=1}^{M} \phi_k\,\psi_k\,\Delta s,$$

respectively. Thus, the total energy is $E = K + B$.

THEOREM 4.1. *The BE scheme of* (4.2)–(4.8) *is unconditionally energy stable; that is, the scheme satisfies* $E^{n+1} \leq E^n$ *for each time-step $n$.*

*Proof.* Taking the discrete inner product of (4.2) with $\mathbf{u}^{n+1} + \mathbf{u}^n$, we obtain

$$\begin{aligned}
K^{n+1}-K^n &= \frac{\rho}{2}\langle\mathbf{u}^{n+1},\mathbf{u}^{n+1}\rangle_{\Omega_h} - \frac{\rho}{2}\langle\mathbf{u}^n,\mathbf{u}^n\rangle_{\Omega_h} \\
&= \frac{\rho}{2}\langle\mathbf{u}^{n+1}+\mathbf{u}^n,\mathbf{u}^{n+1}-\mathbf{u}^n\rangle_{\Omega_h} \\
&= \frac{\rho}{2}\left(-\langle\mathbf{u}^{n+1}-\mathbf{u}^n,\mathbf{u}^{n+1}-\mathbf{u}^n\rangle_{\Omega_h} + 2\langle\mathbf{u}^{n+1},\mathbf{u}^{n+1}-\mathbf{u}^n\rangle_{\Omega_h}\right) \\
&= -\frac{\rho}{2}\|\mathbf{u}^{n+1}-\mathbf{u}^n\|_{\Omega_h}^2 + \langle\mathbf{u}^{n+1},\rho\left(\mathbf{u}^{n+1}-\mathbf{u}^n\right)\rangle_{\Omega_h} \\
&= -\frac{\rho}{2}\|\mathbf{u}^{n+1}-\mathbf{u}^n\|_{\Omega_h}^2 + \Delta t\langle\mathbf{u}^{n+1},-\nabla_h p^{n+1}+\mu\Delta_h\mathbf{u}^{n+1} \\
&\quad + S_h^n(\mathbf{F}_\sigma^{n+1}) + S_h^n(\mathbf{F}_b^{n+1})\rangle_{\Omega_h}.
\end{aligned}$$

Due to the discrete incompressibility condition (4.3) and the discrete inextensibility condition (4.7), the terms of the pressure and the elastic tension are canceled out. Precisely, we have $\langle\mathbf{u}^{n+1},-\nabla_h p^{n+1}\rangle_{\Omega_h} = 0$ (the proof can be performed easily by using the condition (4.3) and the summation by parts) and $\langle\mathbf{u}^{n+1},S_h^n(\mathbf{F}_\sigma^{n+1})\rangle_{\Omega_h} = -\langle\sigma^{n+1},\nabla_{s_h}\cdot\mathbf{U}^{n+1}\rangle_{\Gamma_h} = 0$ (the proof can be found in [21]). Thus, the above equation becomes

$$K^{n+1}-K^n = -\frac{\rho}{2}\|\mathbf{u}^{n+1}-\mathbf{u}^n\|_{\Omega_h}^2 + \mu\Delta t\langle\mathbf{u}^{n+1},\Delta_h\mathbf{u}^{n+1}\rangle_{\Omega_h} + \Delta t\langle\mathbf{u}^{n+1},S_h^n(\mathbf{F}_b^{n+1})\rangle_{\Omega_h}$$

$$(4.18) \qquad = -\frac{\rho}{2}\|\mathbf{u}^{n+1}-\mathbf{u}^n\|_{\Omega_h}^2 - \mu\Delta t\langle\nabla_h\mathbf{u}^{n+1},\nabla_h\mathbf{u}^{n+1}\rangle_{\Omega_h} + \Delta t\langle\mathbf{u}^{n+1},S_h^n(\mathbf{F}_b^{n+1})\rangle_{\Omega_h}.$$

Now we need to compute the last term $\langle\mathbf{u}^{n+1},S_h^n(\mathbf{F}_b^{n+1})\rangle_{\Omega_h}$,

$$\begin{aligned}
\langle\mathbf{u}^{n+1},S_h^n(\mathbf{F}_b^{n+1})\rangle_{\Omega_h} &= \sum_{\mathbf{x}}\left(-c_b\sum_{k=1}^{M} D_s^+ D_s^- D_s^+ D_s^- \mathbf{X}_k^{n+1}\,\delta_h(\mathbf{x}-\mathbf{X}_k^n)\Delta s\right)\cdot\mathbf{u}^{n+1}(\mathbf{x})\,h^2 \\
&= -c_b\sum_{k=1}^{M} D_s^+ D_s^- D_s^+ D_s^- \mathbf{X}_k^{n+1}\cdot\left(\sum_{\mathbf{x}}\mathbf{u}^{n+1}(\mathbf{x})\delta_h(\mathbf{x}-\mathbf{X}_k^n)\,h^2\right)\Delta s \\
&= -c_b\sum_{k=1}^{M} D_s^+ D_s^- D_s^+ D_s^- \mathbf{X}_k^{n+1}\cdot\mathbf{U}_k^{n+1}\,\Delta s
\end{aligned}$$

$$= -c_b \langle D_s^+ D_s^- D_s^+ D_s^- \mathbf{X}^{n+1}, \mathbf{U}^{n+1} \rangle_{\Gamma_h}$$

$$(4.19) \qquad = -c_b \langle D_s^+ D_s^- \mathbf{X}^{n+1}, D_s^+ D_s^- \mathbf{U}^{n+1} \rangle_{\Gamma_h}.$$

Note that the last identity is obtained by $\langle D_s^+ \phi, \psi \rangle_{\Gamma_h} = -\langle \phi, D_s^- \psi \rangle_{\Gamma_h}$ using the fact of summation by parts and the periodicity of the $\Gamma_h$.

The discrete bending energy is

$$\begin{aligned}
B^{n+1} - B^n &= \frac{c_b}{2} \langle D_s^+ D_s^- \mathbf{X}^{n+1}, D_s^+ D_s^- \mathbf{X}^{n+1} \rangle_{\Gamma_h} - \frac{c_b}{2} \langle D_s^+ D_s^- \mathbf{X}^n, D_s^+ D_s^- \mathbf{X}^n \rangle_{\Gamma_h} \\
&= \frac{c_b}{2} \langle D_s^+ D_s^- (\mathbf{X}^{n+1} + \mathbf{X}^n), D_s^+ D_s^- (\mathbf{X}^{n+1} - \mathbf{X}^n) \rangle_{\Gamma_h} \\
&= -\frac{c_b}{2} \langle D_s^+ D_s^- (\mathbf{X}^{n+1} - \mathbf{X}^n), D_s^+ D_s^- (\mathbf{X}^{n+1} - \mathbf{X}^n) \rangle_{\Gamma_h} \\
&\quad + c_b \langle D_s^+ D_s^- \mathbf{X}^{n+1}, D_s^+ D_s^- (\mathbf{X}^{n+1} - \mathbf{X}^n) \rangle_{\Gamma_h} \\
&= -\frac{c_b}{2} \| D_s^+ D_s^- (\mathbf{X}^{n+1} - \mathbf{X}^n) \|_{\Gamma_h}^2 + c_b \langle D_s^+ D_s^- \mathbf{X}^{n+1}, D_s^+ D_s^- (\mathbf{X}^{n+1} - \mathbf{X}^n) \rangle_{\Gamma_h} \\
&= -\frac{c_b}{2} \| D_s^+ D_s^- (\mathbf{X}^{n+1} - \mathbf{X}^n) \|_{\Gamma_h}^2 + c_b \Delta t \langle D_s^+ D_s^- \mathbf{X}^{n+1}, D_s^+ D_s^- \mathbf{U}^{n+1} \rangle_{\Gamma_h} \\
&= -\frac{c_b}{2} \| D_s^+ D_s^- (\mathbf{X}^{n+1} - \mathbf{X}^n) \|_{\Gamma_h}^2 - \Delta t \langle \mathbf{u}^{n+1}, S_h^n (\mathbf{F}_b^{n+1}) \rangle_{\Omega_h} \text{ (by (4.19))}.
\end{aligned}$$

Thus, the total energy between two successive time-steps can be written as

$$(4.20)$$
$$E^{n+1} - E^n = -\frac{\rho}{2} \| \mathbf{u}^{n+1} - \mathbf{u}^n \|_{\Omega_h}^2 - \mu \Delta t \| \nabla_h \mathbf{u}^{n+1} \|_{\Omega_h}^2 - \frac{c_b}{2} \| D_s^+ D_s^- (\mathbf{X}^{n+1} - \mathbf{X}^n) \|_{\Gamma_h}^2.$$

Thus, the total energy is decreasing, which shows the present BE scheme is unconditionally energy stable. □

THEOREM 4.2. *The CN scheme of* (4.9)–(4.15) *is unconditionally energy stable; that is, the scheme satisfies* $E^{n+1} \leq E^n$ *for each time-step* $n$.

*Proof.* Taking the discrete inner product of (4.9) with $\mathbf{u}^{n+1} + \mathbf{u}^n$, we obtain

$$\begin{aligned}
K^{n+1} - K^n &= \frac{\rho}{2} \langle \mathbf{u}^{n+1}, \mathbf{u}^{n+1} \rangle_{\Omega_h} - \frac{\rho}{2} \langle \mathbf{u}^n, \mathbf{u}^n \rangle_{\Omega_h} \\
&= \frac{\rho}{2} \langle \mathbf{u}^{n+1} + \mathbf{u}^n, \mathbf{u}^{n+1} - \mathbf{u}^n \rangle_{\Omega_h} \\
&= \frac{\Delta t}{2} \langle \mathbf{u}^{n+1} + \mathbf{u}^n, -\nabla_h p^{n+1/2} \rangle_{\Omega_h} + \frac{\mu \Delta t}{4} \langle \mathbf{u}^{n+1} + \mathbf{u}^n, \Delta_h (\mathbf{u}^{n+1} + \mathbf{u}^n) \rangle_{\Omega_h} \\
&\quad + \frac{\Delta t}{2} \langle \mathbf{u}^{n+1} + \mathbf{u}^n, S_h^{n-1/2} (\mathbf{F}_\sigma^{n+1/2}) \rangle_{\Omega_h} + \frac{\Delta t}{2} \langle \mathbf{u}^{n+1} + \mathbf{u}^n, S_h^{n-1/2} (\mathbf{F}_b^{n+1/2}) \rangle_{\Omega_h} \\
&= -\frac{\mu \Delta t}{4} \| \nabla_h (\mathbf{u}^{n+1} + \mathbf{u}^n) \|_{\Omega_h}^2 + \frac{\Delta t}{2} \langle \mathbf{u}^{n+1} + \mathbf{u}^n, S_h^{n-1/2} (\mathbf{F}_b^{n+1/2}) \rangle_{\Omega_h},
\end{aligned}$$

where the pressure term satisfies $\langle \mathbf{u}^{n+1} + \mathbf{u}^n, -\nabla_h p^{n+1/2} \rangle_{\Omega_h} = 0$ by using (4.10) and $\nabla_h \cdot \mathbf{u}^n = 0$, and the elastic tension term satisfies

$$\begin{aligned}
\langle \mathbf{u}^{n+1} + \mathbf{u}^n, S_h^{n-1/2} (\mathbf{F}_\sigma^{n+1/2}) \rangle_{\Omega_h} &= -\sum_{k=1}^M \sigma_{k-1/2}^{n+1/2} \boldsymbol{\tau}_{k-1/2}^{n-1/2} \cdot D_s^- \mathbf{U}_k^{n+1/2} \Delta s \\
(4.21) \qquad &= -\langle \sigma^{n+1/2}, \nabla_{s_h} \cdot \mathbf{U}^{n+1/2} \rangle_{\Gamma_h} = 0.
\end{aligned}$$

The proof of above equality can be easily extended from the derivation in [21].

Now we need to compute the last term $\langle \mathbf{u}^{n+1} + \mathbf{u}^n, S_h^{n-1/2}(\mathbf{F}_b^{n+1/2})\rangle_{\Omega_h}$,

$$
\begin{aligned}
&\langle \mathbf{u}^{n+1} + \mathbf{u}^n, S_h^{n-1/2}(\mathbf{F}_b^{n+1/2})\rangle_{\Omega_h} \\
&= \sum_{\mathbf{x}} \left( -c_b \sum_{k=1}^{M} D_s^+ D_s^- D_s^+ D_s^- \mathbf{X}_k^{n+1/2} \, \delta_h(\mathbf{x} - \mathbf{X}_k^{n-1/2})\Delta s \right) \cdot (\mathbf{u}^{n+1}(\mathbf{x}) + \mathbf{u}^n(\mathbf{x})) \, h^2 \\
&= -c_b \sum_{k=1}^{M} D_s^+ D_s^- D_s^+ D_s^- \mathbf{X}_k^{n+1/2} \cdot \left( \sum_{\mathbf{x}} (\mathbf{u}^{n+1}(\mathbf{x}) + \mathbf{u}^n(\mathbf{x}))\delta_h(\mathbf{x} - \mathbf{X}_k^{n-1/2}) \, h^2 \right) \Delta s \\
&= -2c_b \sum_{k=1}^{M} D_s^+ D_s^- D_s^+ D_s^- \mathbf{X}_k^{n+1/2} \cdot \mathbf{U}_k^{n+1/2} \, \Delta s \quad \text{(by (4.13))} \\
&= -2c_b \langle D_s^+ D_s^- D_s^+ D_s^- \mathbf{X}^{n+1/2}, \mathbf{U}^{n+1/2}\rangle_{\Gamma_h} \\
&= -2c_b \langle D_s^+ D_s^- \mathbf{X}^{n+1/2}, D_s^+ D_s^- \mathbf{U}^{n+1/2}\rangle_{\Gamma_h}.
\end{aligned}
$$
(4.22)

Note that the last identity is obtained by applying $\langle D_s^+ \phi, \psi\rangle_{\Gamma_h} = -\langle \phi, D_s^- \psi\rangle_{\Gamma_h}$ twice again. The discrete bending energy is

$$
\begin{aligned}
B^{n+1} - B^n &= \frac{c_b}{2}\langle D_s^+ D_s^- \mathbf{X}^{n+1}, D_s^+ D_s^- \mathbf{X}^{n+1}\rangle_{\Gamma_h} - \frac{c_b}{2}\langle D_s^+ D_s^- \mathbf{X}^n, D_s^+ D_s^- \mathbf{X}^n\rangle_{\Gamma_h} \\
&= \frac{c_b}{2}\langle D_s^+ D_s^- (\mathbf{X}^{n+1} + \mathbf{X}^n), D_s^+ D_s^- (\mathbf{X}^{n+1} - \mathbf{X}^n)\rangle_{\Gamma_h} \\
&= c_b \Delta t \langle D_s^+ D_s^- \mathbf{X}^{n+1/2}, D_s^+ D_s^- \mathbf{U}^{n+1/2}\rangle_{\Gamma_h} \\
&= -\frac{\Delta t}{2}\langle \mathbf{u}^{n+1} + \mathbf{u}^n, S_h^{n-1/2}(\mathbf{F}_b^{n+1/2})\rangle_{\Omega_h} \quad \text{(by (4.22))}.
\end{aligned}
$$

Thus the successive difference of total energy reads

$$
(4.23) \qquad E^{n+1} - E^n = -\frac{\mu \Delta t}{4}\|\nabla_h(\mathbf{u}^{n+1} + \mathbf{u}^n)\|_{\Omega_h}^2,
$$

which shows that the present CN scheme is unconditionally energy stable. Comparing (4.20) and (4.23), the present BE scheme is more energy dissipative than the CN scheme. □

## 5. Numerical method.

**5.1. Linear solver.** The resultant linear system for the BE scheme (equations (4.2)–(4.8)) is expressed as

$$
(5.1) \qquad
\begin{bmatrix}
\left(\frac{\rho}{\Delta t}I - \mu\Delta_h\right) & \nabla_h & -S_\sigma & -S_b \\
\nabla_h^T & 0 & 0 & 0 \\
-S_\sigma^T & 0 & 0 & 0 \\
-I_h & 0 & 0 & \frac{1}{\Delta t}I
\end{bmatrix}
\begin{bmatrix}
\mathbf{u}^{n+1} \\
p^{n+1} \\
\sigma^{n+1} \\
\mathbf{X}^{n+1}
\end{bmatrix}
=
\begin{bmatrix}
\frac{\rho}{\Delta t}\mathbf{u}^n \\
0 \\
0 \\
\frac{1}{\Delta t}\mathbf{X}^n
\end{bmatrix}.
$$

Likewise, the resultant linear system for the CN scheme (equations (4.9)–(4.15)) is expressed as

(5.2)
$$
\begin{bmatrix}
\left(\frac{\rho}{\Delta t}I - \frac{\mu}{2}\Delta_h\right) & \nabla_h & -S_\sigma & -\frac{1}{2}S_b \\
\nabla_h^T & 0 & 0 & 0 \\
-S_\sigma^T & 0 & 0 & 0 \\
-\frac{1}{2}I_h & 0 & 0 & \frac{1}{\Delta t}I
\end{bmatrix}
\begin{bmatrix}
\mathbf{u}^{n+1} \\
p^{n+1/2} \\
\sigma^{n+1/2} \\
\mathbf{X}^{n+1}
\end{bmatrix}
=
\begin{bmatrix}
\left(\frac{\rho}{\Delta t}I + \frac{\mu}{2}\Delta_h\right)\mathbf{u}^n + \frac{1}{2}S_b(\mathbf{X}^n) \\
0 \\
S_\sigma^T(\mathbf{u}^n) \\
\frac{1}{\Delta t}\mathbf{X}^n + \frac{1}{2}I_h(\mathbf{u}^n)
\end{bmatrix}.
$$

In the staggered grid discretization framework, the discrete divergence operator of the fluid velocity can be written as the transpose of the discrete gradient operator of the pressure. Furthermore, the discrete surface divergence operator of the velocity can be written as the transpose of the discrete spreading operator of the elastic tension [21]. At each time-step, the operator $S_\sigma$, $S_\sigma^T$, $S_b$, and $I_h$ are updated, as well as the corresponding source terms. Notice that in the case of no-slip boundary conditions being used, there will be an extra term in the right-hand side arising from the boundary conditions for $\mathbf{u}^{n+1}$.

There are several possible methods for solving the unsymmetric sparse linear systems (5.1) and (5.2). The straightforward strategy is to apply Krylov subspace methods directly, such as GMRES and BICGSTAB. However, it is very likely that these sparse iterative linear solvers may fail to converge without an efficient preconditioner. Another one is based on the double Schur complement [9, 7, 12] to which Krylov subspace methods can be applied subsequently. It is realized that this approach also suffers from a lack of efficient preconditioners on top of operator splitting errors. As a consequence, semi-implicit IB schemes with iterative linear solvers may be more computationally expensive than the explicit IB methods. For the same simulation time, they may need more iterations to solve the linear system at a given time-step than the number of time-steps that would be required by the explicit IB schemes, although they grant a larger time-step than explicit IB methods [7, 12].

In the present study, the unsymmetric sparse linear systems (5.1) and (5.2) are solved directly using the unsymmetric multifrontal method [31]. We assign the pressure value at the first grid point to remove the rank deficiency of the system due to the nonuniqueness of the pressure. As far as we are concerned, the option of semi-implicit IB schemes with sparse direct linear solvers has not been explored. The primary advantages of direct solvers are highly robust and accurate. They do not require any preconditioners, and they eliminate the need for any iterations within each time-step, and hence convergence analysis. On the other hand, the major deficiencies of sparse direct solvers are the programming complexity including explicit matrix entries at each time-step, and the numerical LU factorization would lead to a large amount of fill-in which occupies a large amount of computer memory. These shortcomings are outweighed by their advantages over sparse iterative linear solvers for the present unconditionally energy stable schemes to solve the inextensible interface problem with bending. Furthermore, semi-implicit IB schemes with sparse direct linear solvers could serve as an important benchmark for developing potential fast solvers and efficient preconditioners in the future.

**5.2. Initial arc-length parametrization.** In the present study, our initial interface is always chosen as an ellipse so the initial arc-length parametrization is needed. Let us consider the ellipse be parameterized by $\mathbf{X}_k = (X_k, Y_k) = (a\cos\theta_k, b\sin\theta_k)$, $k = 0, 1, \ldots M - 1$, where $a$ is the semiminor axis and $b$ is the semimajor axis. Henceforth, the total arc-length $L$ of the ellipse is given by

$$L = 4b \int_0^{\pi/2} \sqrt{1 - e^2 \sin^2 \theta} \, \mathrm{d}\theta = 4b E_m(e),$$

where $E_m(e)$ is the complete elliptic integral of the second kind and $e = \sqrt{1 - (a/b)^2}$ is the eccentricity. In the current implementation, $E_m(e)$ is computed numerically using the piecewise minimax rational function approximation [32]. Since an ellipse is fourfold symmetry, we first compute the position vector $(X_k, Y_k)$ of discrete points $s_k$ with uniform arc-length on the first quadrant. Then the discrete points $s_k$ on the other quadrants can be obtained subsequently. Let

$$q_k = k \frac{E_m(e)}{M/4}, \quad k = 0, 1, \ldots M/4 - 1,$$

the corresponding $\theta_k$ is therefore given by $\theta_k = E_m^{-1}(q_k, e)$. The inversion of the incomplete elliptic integral of the second kind $E_m^{-1}(q_k, e)$ with respect to $\theta_k$ can be evaluated by solving the transcendental equation $E_m(\theta_k, e) - q_k = 0$ with the Newton–Raphson method [33], i.e.,

$$(5.3) \qquad \theta_k^{l+1} = \theta_k^l - \frac{E_m(\theta_k^l, e) - q_k}{\sqrt{1 - e^2 \sin^2 \theta_k^l}},$$

where $l$ is the iteration index and $E_m(\theta, e)$ is the incomplete elliptic integral of the second kind which is evaluated numerically by the half and double argument transformations [34]. Practically, the solution of (5.3) converges to $\theta_k = E_m^{-1}(q_k, e)$ within an error tolerance of $10^{-12}$ in five iterations. The overall procedure only requires it to be carried out at the initialization stage before the time-marching simulation, and it only imposes a negligible computation overhead.

**5.3. Nonuniform fourth derivative operator.** The exact inextensibility constraint (2.6) requires the initial uniform arc-length mesh to be always fixed as time proceeds. However, in practical simulations, the immersed interface is observed to elongate or shrink sluggishly, i.e., the distribution of discrete points $s_k$ with uniform arc-length will not be sustainable. Consequently, the uniform fourth derivative operator $D_s^+ D_s^- D_s^+ D_s^- \phi_k$ used in (4.5) for the BE scheme and in (4.12) for the CN scheme should be modified accordingly with respect to local discrete arc-length $\Delta s_k$.

Here, we define the nonuniform fourth derivative operator based on Taylor series expansion,

$$\frac{\partial^4 \phi_k}{\partial s^4} \approx \sum_{p=-2}^{2} c_{k+p} \phi_{k+p}$$

$$(5.4) \qquad = c_{k-2} \phi_{k-2} + c_{k-1} \phi_{k-1} + c_k \phi_k + c_{k+1} \phi_{k+1} + c_{k+2} \phi_{k+2},$$

where the stencil coefficients are given by

$$c_{k-2} = \frac{24}{\Delta s_{k-2}(\Delta s_{k-2} + \Delta s_{k-1})(\Delta s_{k-2} + \Delta s_{k-1} + \Delta s_k)(\Delta s_{k-2} + \Delta s_{k-1} + \Delta s_k + \Delta s_{k+1})},$$

$$c_{k-1} = -\frac{24}{\Delta s_{k-2} \Delta s_{k-1}(\Delta s_{k-1} + \Delta s_k)(\Delta s_{k-1} + \Delta s_k + \Delta s_{k+1})},$$

$$c_k = \frac{24}{\Delta s_{k-1} \Delta s_k (\Delta s_{k-2} + \Delta s_{k-1})(\Delta s_k + \Delta s_{k+1})},$$

$$c_{k+1} = -\frac{24}{\Delta s_k \Delta s_{k+1}(\Delta s_{k-1} + \Delta s_k)(\Delta s_{k-2} + \Delta s_{k-1} + \Delta s_k)},$$

$$c_{k+2} = \frac{24}{\Delta s_{k-2}(\Delta s_k + \Delta s_{k+1})(\Delta s_{k-1} + \Delta s_k + \Delta s_{k+1})(\Delta s_{k-2} + \Delta s_{k-1} + \Delta s_k + \Delta s_{k+1})}.$$

At each time-step, the local arc-length $\Delta s_k$ is evaluated and the stencil coefficients are updated. Note that (5.4) is equivalent to $D_s^+ D_s^- D_s^+ D_s^- \phi_k$ when the local arc-length $\Delta s_k = \Delta s$ is uniform. More precisely, for the uniform arc-length mesh, (5.4) becomes

$$(5.5) \qquad \frac{\partial^4 \phi_k}{\partial s^4} \approx \frac{\phi_{k-2} - 4\phi_{k-1} + 6\phi_k - 4\phi_{k+1} + \phi_{k+2}}{\Delta s^4} \equiv D_s^+ D_s^- D_s^+ D_s^- \phi_k.$$

Since the interface is closed, the interfacial markers $\mathbf{X}_k, k = 0, 1, \ldots M - 1$, are periodic. Thus, the periodic boundary condition can be applied to the above difference formula as $\phi_k = \phi_{k(mod)M}$. For instance, at $k = 0$, the fourth-order derivative is calculated as

$$\frac{\partial^4 \phi_0}{\partial s^4} \approx c_{M-2}\phi_{M-2} + c_{M-1}\phi_{M-1} + c_0\phi_0 + c_1\phi_1 + c_2\phi_2.$$

Similar treatments are also applied to the points at $k = 1, M - 2, M - 1$.

**5.4. Discrete delta function.** The two-dimensional discrete delta function is represented by a tensor product of a kernel $\psi(r)$,

$$(5.6) \qquad \delta_h(\mathbf{x}) = \frac{1}{h^2} \psi\left(\frac{x}{h}\right) \psi\left(\frac{y}{h}\right).$$

We employ the following kernel $\psi(r)$ [35]:
(5.7)
$$\psi(r) = \begin{cases} \frac{3}{8} + \frac{\pi}{32} - \frac{r^2}{4}, & |r| < 0.5, \\ \frac{1}{4} + \frac{1-|r|}{8}\sqrt{-2 + 8|r| - 4r^2} - \frac{1}{8}\sin^{-1}\left(\sqrt{2}\,(|r| - 1)\right), & 0.5 \leq |r| < 1.5, \\ \frac{17}{16} - \frac{\pi}{64} - \frac{3|r|}{4} + \frac{r^2}{8} + \frac{|r|-2}{16}\sqrt{-14 + 16|r| - 4r^2} & \\ \quad + \frac{1}{16}\sin^{-1}\left(\sqrt{2}\,(|r| - 2)\right), & 1.5 \leq |r| \leq 2.5, \\ 0, & 2.5 \leq |r|. \end{cases}$$

Equation (5.7) holds the advantage of suppressing numerical wiggles in the vicinity of an interface caused by the IB method. We remark that various discrete delta functions have also been utilized in the IB method, and the development of the discrete delta function is an area of active research [36].

**6. Numerical results.**

**6.1. Energy stability check.** We first conduct a simple energy stability check for the present BE and CN IB schemes developed in section 4. We set an initial vesicle shape as an ellipse $\mathbf{X}(\theta) = (0.2\cos\theta, 0.5\sin\theta)$ which is immersed in a quiescent fluid domain $\Omega = [0, 2] \times [0, 2]$. For other parameters, we set $\rho = 1$, $\mu = 1$, and $c_b = 0.01$. The simulations are time-marched from time $t = 0$ to $t = 3.0$ with a fixed mesh size of $h = 1/128$ but differ on time-step sizes $\Delta t = 2h$, $h$, $h/2$, $h^2$ to check the numerical stability. We choose the number of Lagrangian markers $M$ such that $\Delta s$ is proportional to $h$. One should be aware that the choice of the ratio $\Delta s/h$ is not exhaustive, and it is usually a localized problem-dependent parameter. Nevertheless, the current choice is realized to be one of the optimum ratios that are achieving the desired accuracy without compromising both the area conservation and total arc-length conservation, as well as alleviating the potential numerical wiggles, particularly on the solution of pressure and elastic tension in the vicinity of the interface.

Figure 1 shows the transient dissipation profiles of total energy $E$ normalized by initial total energy $E_0$ at $t = 0$. Both BE and CN produce consistent and nearly identical results. The total energy profiles are monotonically decreasing, which substantiates that present BE and CN schemes are unconditionally energy stable. Figure 2 depicts
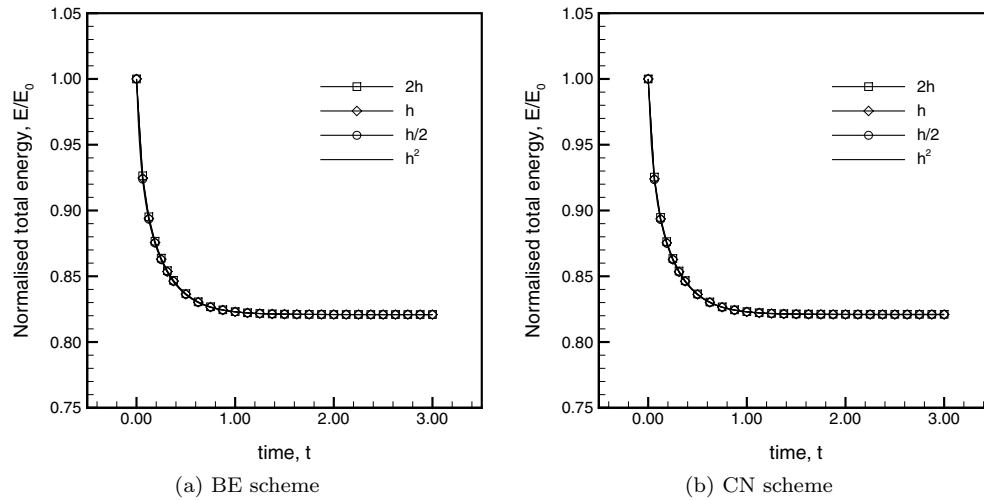
FIG. 1. *Normalized total energy $E/E_0$ dissipation profiles from time $t = 0$ to $t = 3.0$ with a fixed mesh size of $h = 1/128$ and different time-step sizes $\Delta t = 2h, h, h/2, h^2$.*

the vesicle shapes and elastic tension profiles of the BE scheme and the CN scheme at $t = 3.0$ using the mesh of $h = 1/128$ and $\Delta t = h^2$. The simulation results of the BE scheme and the CN scheme are congruent to each other qualitatively. It is worth mentioning that the initial arc-length parametrization is able to alleviate the numerical wiggles in the computed elastic tension as observed in [37, 20, 38]. In the following subsection, we further investigate the convergence rate of solution variables quantitatively.

**6.2. Grid convergence study 1: Vesicle in a quiescent flow.** It is well-known that the IB method is usually limited to first-order accurate regardless of the choice of fluid solvers. Therefore, in the remainder of this paper, we only focus on the numerical results computed by BE scheme. First, we perform the grid convergence study for the vesicle in a quiescent flow. Similar to the previous case, we set an initial vesicle shape given by an ellipse $\mathbf{X}(\theta) = (0.2\cos\theta, 0.5\sin\theta)$, immersed in a quiescent fluid domain $\Omega = [0, 2] \times [0, 2]$. For a linear refinement, we use the time-step of $\Delta t = h = 2/m$ and differ the grid number $m = n = 64, 128, 256$, and $512$. Since the analytical solution is not available here, we use the numerical solution obtained from the finest grid $m = n = 512$ as the reference solution and compute the error by the difference between the computed and reference solutions. All the simulations are computed from time $t = 0$ to $t = 3.0$.

Table 1 shows the grid refinement analysis of the BE scheme on the solution variables, i.e., velocity components $u$ and $v$, Lagrangian markers $X$ and $Y$, and elastic tension $\sigma$. The numerical results indicate that the rate of convergence is between first- and second-order for all solution variables except for the elastic tension $\sigma$, which is approximately first-order convergence. The grid convergence study shows slightly better accuracy than the formal order of accuracy primarily due to the adoption of the interpolated numerical solution from a fine mesh as the reference solution, since the analytical solution is not available. In the authors' practical experience, the numerical results for the interface problems very often do not show clean order of accuracy, especially when the interface is moving. Next, we examine the grid convergence of the enclosed area $A$ and total arc-length $L$ to investigate the scheme's
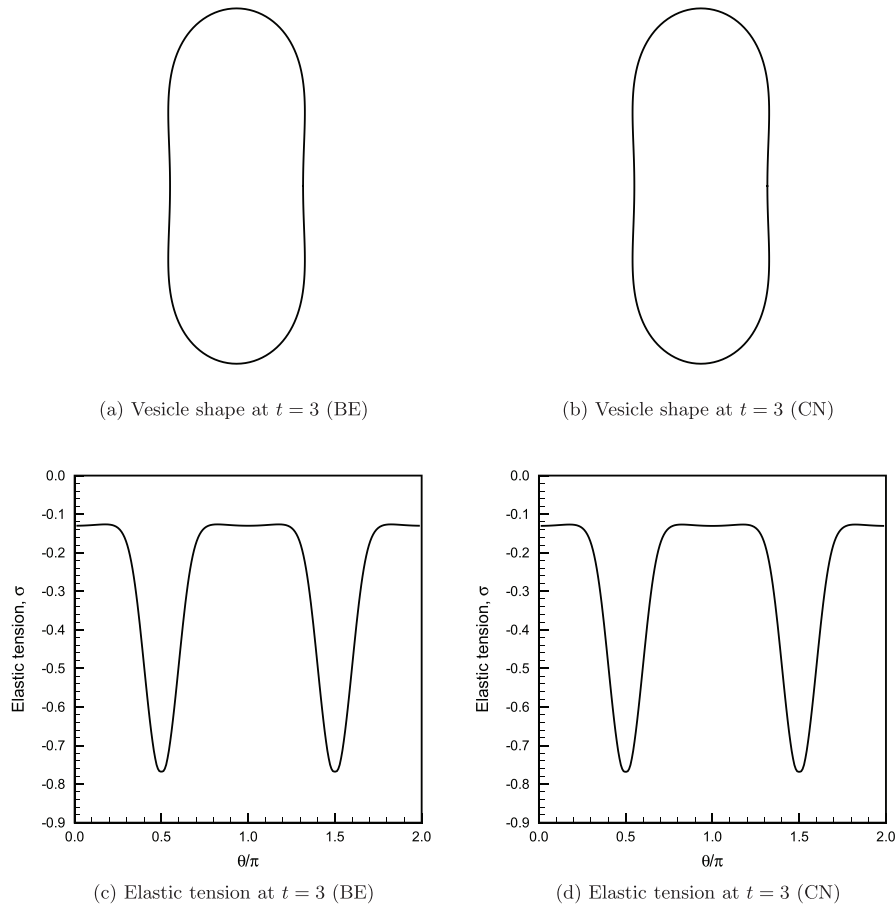
(a) Vesicle shape at $t = 3$ (BE)          (b) Vesicle shape at $t = 3$ (CN)

(c) Elastic tension at $t = 3$ (BE)         (d) Elastic tension at $t = 3$ (CN)

FIG. 2. *Vesicle shapes and elastic tension profiles of BE scheme and CN scheme.*

TABLE 1
*Grid convergence study* 1*: grid refinement analysis of BE scheme on the velocity components $u$ and $v$, Lagrangian markers $X$ and $Y$, and elastic tension $\sigma$.*

|  | $m = n = 64$ | $m = n = 128$ | Rate | $m = n = 256$ | Rate |
|---|---|---|---|---|---|
| $\|u_h - u_{\mathrm{ref}}\|_\infty$ | $1.852 \times 10^{-4}$ | $5.267 \times 10^{-5}$ | 1.81 | $1.967 \times 10^{-5}$ | 1.42 |
| $\|v_h - v_{\mathrm{ref}}\|_\infty$ | $1.699 \times 10^{-4}$ | $4.804 \times 10^{-5}$ | 1.82 | $1.610 \times 10^{-5}$ | 1.58 |
| $\|X_h - X_{\mathrm{ref}}\|_\infty$ | $9.677 \times 10^{-4}$ | $2.133 \times 10^{-4}$ | 2.18 | $3.990 \times 10^{-5}$ | 2.42 |
| $\|Y_h - Y_{\mathrm{ref}}\|_\infty$ | $1.222 \times 10^{-3}$ | $3.585 \times 10^{-4}$ | 1.77 | $9.181 \times 10^{-5}$ | 1.97 |
| $\|\sigma_h - \sigma_{\mathrm{ref}}\|_\infty$ | $5.331 \times 10^{-2}$ | $2.988 \times 10^{-2}$ | 0.83 | $1.504 \times 10^{-2}$ | 0.99 |

capability of preserving these quantities. Table 2 summarizes the grid refinement analysis of these physical parameters. Here, $A_0$ and $L_0$ are the initial enclosed area and initial total arc-length of the vesicle, respectively. Table 2 shows that these relative errors are gradually decreased at an approximately first-order rate as the grid is refined. Furthermore, the relative errors show that the percentage of area loss and total arc-length loss are about 0.001% and 0.01%, respectively, when the grid $m = n = 256$ is used. One can conclude that our present scheme preserves the total area and total arc-length comparably well numerically.

TABLE 2

*Grid convergence study* 1: *grid refinement analysis of BE scheme on the enclosed area A, and total arc-length L.*

|  | $m = n = 64$ | $m = n = 128$ | Rate | $m = n = 256$ | Rate |
|---|---|---|---|---|---|
| $|A_h - A_0|/A_0$ | $7.561 \times 10^{-5}$ | $3.001 \times 10^{-5}$ | 1.33 | $1.395 \times 10^{-5}$ | 1.11 |
| $|L_h - L_0|/L_0$ | $3.252 \times 10^{-4}$ | $2.590 \times 10^{-4}$ | 0.33 | $1.553 \times 10^{-4}$ | 0.74 |

TABLE 3

*Grid convergence study* 2: *grid refinement analysis of BE scheme on the velocity components u and v, Lagrangian markers X and Y, and elastic tension $\sigma$.*

|  | $m = n = 64$ | $m = n = 128$ | Rate | $m = n = 256$ | Rate |
|---|---|---|---|---|---|
| $\|u_h - u_{\mathrm{ref}}\|_\infty$ | $8.872 \times 10^{-2}$ | $3.141 \times 10^{-2}$ | 1.50 | $1.078 \times 10^{-2}$ | 1.54 |
| $\|v_h - v_{\mathrm{ref}}\|_\infty$ | $6.210 \times 10^{-2}$ | $2.831 \times 10^{-2}$ | 1.13 | $9.326 \times 10^{-3}$ | 1.60 |
| $\|X_h - X_{\mathrm{ref}}\|_\infty$ | $1.078 \times 10^{-1}$ | $3.482 \times 10^{-2}$ | 1.63 | $9.641 \times 10^{-3}$ | 1.85 |
| $\|Y_h - Y_{\mathrm{ref}}\|_\infty$ | $1.132 \times 10^{-1}$ | $3.978 \times 10^{-2}$ | 1.51 | $1.144 \times 10^{-2}$ | 1.80 |
| $\|\sigma_h - \sigma_{\mathrm{ref}}\|_\infty$ | $8.273 \times 10^{-1}$ | $1.959 \times 10^{-1}$ | 2.08 | $5.652 \times 10^{-2}$ | 1.79 |

TABLE 4

*Grid convergence study* 2: *grid refinement analysis of BE scheme on the enclosed area A, total arc-length L, and frequency $\omega$.*

|  | $m = n = 64$ | $m = n = 128$ | Rate | $m = n = 256$ | Rate |
|---|---|---|---|---|---|
| $|A_h - A_0|/A_0$ | $1.228 \times 10^{-2}$ | $8.025 \times 10^{-3}$ | 0.61 | $4.523 \times 10^{-3}$ | 0.83 |
| $|L_h - L_0|/L_0$ | $1.463 \times 10^{-2}$ | $8.419 \times 10^{-3}$ | 0.80 | $4.389 \times 10^{-3}$ | 0.94 |
| $|\omega_h - \omega_{\mathrm{ref}}|$ | $4.809 \times 10^{-2}$ | $1.507 \times 10^{-2}$ | 1.67 | $4.207 \times 10^{-3}$ | 1.84 |

**6.3. Grid convergence study 2: Vesicle in a shear flow.** We now perform the grid convergence study on the BE scheme for the vesicle under shear flow to further justify its numerical behavior under a more complex configuration. We compute the dynamics of a vesicle with an initial shape given by an ellipse $\mathbf{X}(\theta) = (0.2 \cos \theta, 0.5 \sin \theta)$, immersed in a fluid domain $\Omega = [0, 4] \times [0, 4]$ with a shear rate of $\dot{\gamma} = 1$. The parameters are chosen the same as in the previous test. Also, we use the time-step of $\Delta t = h/4 = 1/m$ and differ on the grid number $m = n = 64, 128, 256$, and 512. Since the analytical solution is not available here, we use the numerical solution obtained from the finest grid $m = n = 512$ as the reference solution and compute the error by the difference between the computed and reference solutions. All the simulations are computed from time $t = 0$ to $t = 10.0$.

Table 3 shows the grid refinement analysis of the BE scheme on the solution variables, i.e., velocity components $u$ and $v$, Lagrangian markers $X$ and $Y$, and elastic tension $\sigma$ for the present vesicle under shear flow. Similar to the prior grid convergence study, the numerical results demonstrate that the rate of convergence is between first- and second-order for all the solution variables. Since the vesicle undergoes a tank-treading motion in a shear flow, we examine the grid convergence of the evolution frequency $\omega = 2\pi/\int_\Gamma \frac{dl}{\mathbf{u} \cdot \boldsymbol{\tau}}$, on top of the enclosed area $A$, and total arc-length $L$. Table 4 tabulates the grid refinement analysis of these derived parameters. As the grid is linearly refined, the conservation of the enclosed area and total arc-length of the vesicle are gradually improved at a first-order rate approximately while the evolution frequency converges between first- and second-order rate.
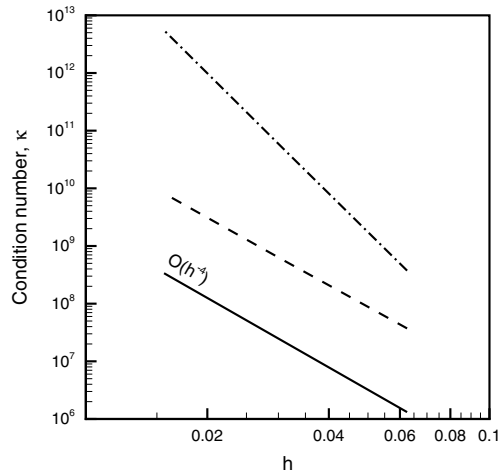
FIG. 3. *Condition number $\kappa$ against mesh width $h$ at $t = 10$: unsteady Stokes system — — —, coupled unsteady Stokes system, and inextensible interface with bending – · – · –.*

We also compute the 1-norm condition number $\kappa$ of the matrix in (5.1) using Hager's algorithm [39] for different grid mesh widths. Since the operator $S_\sigma$, $S_b$, and $I_h$ in the matrix are updated at each time-step due to the moving Lagrangian markers, we only show the condition number versus mesh width at time $t = 10$ in Figure 3 (The results at other times are similar, so we omit them here.). For comparison, we also show the condition number of the pure stationary Stokes system without inextensible interface which is a saddle point problem, and the condition number behaves like $O(h^{-4})$. Since the present model is for Stokes flow with an inextensible interface and bending, the condition number of the resultant matrix expects to be larger than the original pure Stokes system as seen in Figure 3.

**6.4. Tank-treading motion of vesicle in a shear flow.** We now are ready to study the dynamics of a vesicle immersed in a shear flow. Since the exterior fluid and the interior fluid of the vesicle are assumed to be homogeneous ($\rho = 1$, $\mu = 1$), it exhibits a tank-treading motion once it reaches the equilibrium [40, 41, 42]. We define the reduced area $V = A/(\pi R_0)^2$ to classify the vesicle shape with $R_0 = L/2\pi$ the length-scale. To characterize the vesicle dynamics in shear flow, we define the dimensionless shear rate $\chi \equiv \dot{\gamma}\lambda$, where $\lambda = \mu R_0^3/c_b$ is the time-scale. In the present case study, we perform a series of simulations by varying the vesicle reduced area $V = 0.5, 0.6, 0.7, 0.8, 0.9$, and the dimensionless shear rate $\chi = 1, 5, 10$ in a fluid domain $\Omega = [0, 4] \times [0, 4]$. We run the simulations using a time-step of $\Delta t = 0.25(h/\chi)$ and grid number $m = n = 256$. All the simulations are computed up to when the steady state occurs.

Figure 4 depicts the equilibrium vesicle shapes with reduced area of $V = 0.5$, 0.6, 0.7, 0.8, 0.9 under shear flows with dimensionless shear rate of $\chi = 1, 5, 10$. Figure 4 also illustrates the elastic tension $\sigma$ distributions by contour plots of 20 levels. The contour levels are scaled individually for each case with 10 levels in the positive value (red end) representing extension and 10 levels in the negative value (blue end) representing compression, while the inflection points, i.e., $\sigma = 0$, are represented by the black end. We observe that, due to the shear-driven fluid flow, the greatest values of the tension are in the middle of the vesicle for all the cases except the case of $V = 0.5$, $\chi = 1$ (Figure 4(a)). The greatest tension occurs slightly offset from the
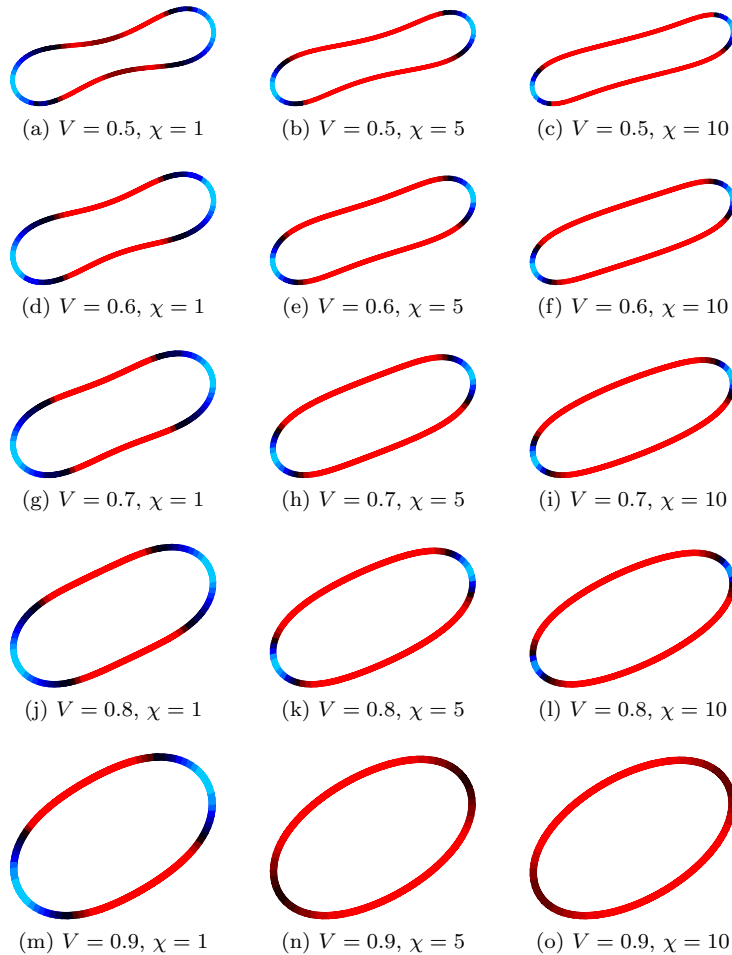
(a) $V = 0.5$, $\chi = 1$      (b) $V = 0.5$, $\chi = 5$      (c) $V = 0.5$, $\chi = 10$

(d) $V = 0.6$, $\chi = 1$      (e) $V = 0.6$, $\chi = 5$      (f) $V = 0.6$, $\chi = 10$

(g) $V = 0.7$, $\chi = 1$      (h) $V = 0.7$, $\chi = 5$      (i) $V = 0.7$, $\chi = 10$

(j) $V = 0.8$, $\chi = 1$      (k) $V = 0.8$, $\chi = 5$      (l) $V = 0.8$, $\chi = 10$

(m) $V = 0.9$, $\chi = 1$      (n) $V = 0.9$, $\chi = 5$      (o) $V = 0.9$, $\chi = 10$

FIG. 4. *The equilibrium vesicle shapes of $V = 0.5$, 0.6, 0.7, 0.8, 0.9 under shear flows of $\chi = 1$, 5, 10. The elastic tension distributions are represented by 20 contour levels. The contour levels are scaled individually with 10 levels in the positive value (red end) representing tension and 10 levels in the negative value (blue end) representing compression, while the inflection point is represented by the black end.*

middle of the vesicle owing to the larger dented profile (biconcave-shaped) compared to the others. On the other hand, the greatest values of the compression occur on both ends of the vesicles parallel to the inclination angle. However, no compression (hence inflection point) is detected for the case $V = 0.9$, $\chi = 5$ (Figure 4(n)) and $V = 0.9$, $\chi = 10$ (Figure 4(o)). Instead, the lowest values of the tension occur on these ends of the vesicle.

Figure 5 plots the inclination angle $\theta/\pi$ and the scaled tank-treading evolution frequency $\omega\lambda/\chi$ of the vesicle in term of reduced area $V$ at their equilibrium shape. It is observed that these two quantities are proportional to the reduced area $V$ but independent of the dimensionless shear rate $\chi$. The present findings are congruent with the literature such as [41, 43, 20].
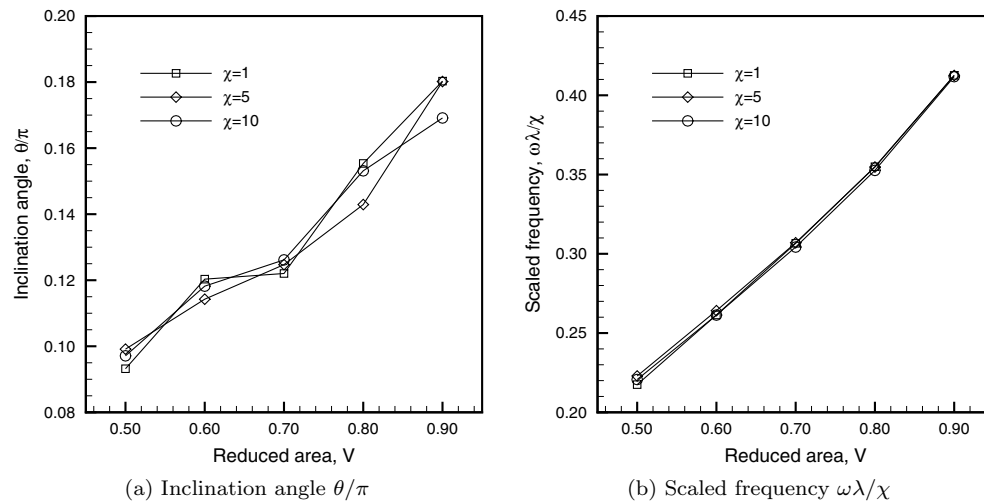
(a) Inclination angle $\theta/\pi$          (b) Scaled frequency $\omega\lambda/\chi$

FIG. 5. *Inclination angle $\theta/\pi$ and scaled tank-treading evolution frequency $\omega\lambda/\chi$ of the vesicle in terms of reduced area $V$ at their equilibrium shape under dimensionless shear rate $\chi = 1$, 5, 10.*

**7. Conclusions.** In the present study, we have developed semi-implicit IB schemes (backward Euler (BE) and Crank–Nicholson (CN) schemes) to solve the inextensible interface problem with bending, that proved to be unconditionally stable, i.e., bounded discrete energy. The fundamental problem is formulated by the nonstationary Stokes equations, in conjunction with the elastic tension force and bending forces defined in terms of Dirac delta function along the interface. The elastic tension acts as a Lagrange multiplier to enforce the inextensibility of the interface which is analogous to the role of pressure to enforce the fluid incompressibility.

For the present semi-implicit IB schemes, the resultant unsymmetric sparse linear systems are solved directly using the unsymmetric multifrontal method. Contrary to the sparse iterative solvers, the sparse direct solvers are robust and accurate and avoid the need for any preconditioners and iterations. These advantages are favored for the present semi-implicit IB schemes and certainly outweigh their shortcomings, i.e., explicit matrix entries and a significant amount of fill-in due to the numerical LU factorization. We suggest that semi-implicit IB methods with sparse direct linear solvers could serve as an important benchmark for the development of potential fast solvers and efficient preconditioners.

We have verified that the proposed BE and CN schemes result in consistent energy stable methods which significantly alleviate the time-step restriction. Furthermore, two grid convergence studies were conducted on the BE scheme. The numerical results indicate that the convergence rates of the solution variables, i.e., velocity components $u$ and $v$, Lagrangian markers $X$ and $Y$, and elastic tension $\sigma$, are between first- and second-order. Since our numerical schemes enforce the discrete inextensibility constraint rather than the exact inextensibility constraint, area and arc-length conservation loss should be perceived in practical simulations. The numerical results show that these errors are gradually decreased at an approximately first-order rate as the grid is linearly refined.

Finally, the BE scheme is applied to study the tank-treading motion of a vesicle immersed in a shear flow. We present the equilibrium vesicle shapes of different reduced area $V$ under different dimensionless shear rate $\chi$, in conjunction with elastic

tension $\sigma$ distribution along the vesicle interfaces. Notably, the numerical wiggles in the computed elastic tension profiles are alleviated effectively. It is also observed that inclination angle $\theta/\pi$ and the scaled tank-treading evolution frequency $\omega\lambda/\chi$ are proportional to the reduced area $V$ but independent of the shear rate $\chi$. These findings are congruent with the previous studies.

## REFERENCES

[1] C. S. Peskin, *Flow patterns around heart valves: a numerical method*, J. Comput. Phys., 10 (1972), pp. 220–252.

[2] C. S. Peskin, *The immersed boundary method*, Acta Numer., 11 (2002), pp. 1–39.

[3] A. M. Roma, C. S. Peskin, and M. J. Berger, *An adaptive version of the immersed boundary method*, J. Comput. Phys., 153 (1999), pp. 509–534.

[4] M.-C. Lai and C. S. Peskin, *An immersed boundary method with formal second-order accuracy and reduced numerical viscosity*, J. Comput. Phys., 160 (2000), pp. 705–719.

[5] B. E. Griffith and C. S. Peskin, *On the order of accuracy of the immersed boundary method: Higher order convergence rates for sufficiently smooth problems*, J. Comput. Phys., 208 (2005), pp. 75–105.

[6] B. E. Griffith, R. D. Hornung, D. M. McQueen, and C. S. Peskin, *An adaptive, formally second order accurate version of the immersed boundary method*, J. Comput. Phys., 223 (2007), pp. 10–49.

[7] Y. Mori and C. S. Peskin, *Implicit second-order immersed boundary methods with boundary mass*, Comput. Methods Appl. Mech. Engrg., 197 (2008), pp. 2049–2067.

[8] C. Tu and C. S. Peskin, *Stability and instability in the computation of flows with moving immersed boundaries: A comparison of three methods*, SIAM J. Sci. Stat. Comput., 13 (1992), pp. 1361–1376.

[9] A. A. Mayo and C. S. Peskin, *An implicit numerical method for fluid dynamics problems with immersed elastic boundaries*, Contemp. Math., 141 (1993), pp. 261–277.

[10] J. M. Stockie and B. R. Wetton, *Analysis of stiffness in the immersed boundary method and implications for time-stepping schemes*, J. Comput. Phys., 154 (1999), pp. 41–64.

[11] E. P. Newren, A. L. Fogelson, R. D. Guy, and R. M. Kirby, *Unconditionally stable discretizations of the immersed boundary equations*, J. Comput. Phys., 222 (2007), pp. 702–719.

[12] E. P. Newren, A. L. Fogelson, R. D. Guy, and R. M. Kirby, *A comparison of implicit solvers for the immersed boundary equations*, Comput. Methods Appl. Mech. Engrg., 197 (2008), pp. 2290–2304.

[13] W.-F. Hu and M.-C. Lai, Unconditionally energy stable immersed boundary method with application to vesicle dynamics, East Asian J. Appl. Math., 3 (2013), pp. 247–262.

[14] T. Y. Hou and Z. Shi, *Removing the stiffness of elastic force from the immersed boundary method for the 2D Stokes equations*, J. Comput. Phys., 227 (2008), pp. 9138–9169.

[15] T. Y. Hou and Z. Shi, *An efficient semi-implicit immersed boundary method for the Navier-Stokes equations*, J. Comput. Phys., 227 (2008), pp. 8968–8991.

[16] H. D. Ceniceros, J. E. Fisher, and A. M. Roma, *Efficient solutions to robust, semi-implicit discretizations of the immersed boundary method* J. Comput. Phys., 228 (2009), pp. 7137–7158.

[17] H. D. Ceniceros and J. E. Fisher, *A fast, robust, and non-stiff immersed boundary method*, J. Comput. Phys., 230 (2011), pp. 5133–5153.

[18] R. D. Guy and B. Philip, *A multigrid method for a model of the implicit immersed boundary equations*, Commun. Comput. Phys., 12 (2012), pp. 378–400.

[19] Q, Zhang, R. D. Guy, and B. Philip, *A projection preconditioner for solving the implicit immersed boundary equations*, Numer. Math. Theoret. Methods Appl., 7 (2014), pp. 473–498.

[20] Y. Kim and M.-C. Lai, *Simulating the dynamics of inextensible vesicles by the penalty immersed boundary method*, J. Comput. Phys., 229 (2010), pp. 4840–4853.

[21] M.-C. Lai, W.-F. Hu, and W.-W. Lin, *A fractional step immersed boundary method for Stokes flow with an inextensible interface enclosing a solid particle*, SIAM J. Sci. Comput., 34 (2012), pp. B692–B710.

[22] T. G. Fai, B. E. Griffith, Y. Mori, and C. S. Peskin, *Immersed boundary method for variable viscosity and variable density problems using fast constant-coefficient linear solvers* I: *Numerical method and results*, SIAM J. Sci. Comput., 35 (2013), pp. B1132–B1161.

[23] T. G. FAI, B. E. GRIFFITH, Y. MORI, AND C. S. PESKIN, *Immersed boundary method for variable viscosity and variable density problems using fast constant-coefficient linear solvers II: Theory*, SIAM J. Sci. Comput., 36 (2014), pp. B589–B621.

[24] W.-F. HU, Y. KIM, AND M.-C. LAI, *An immersed boundary method for simulating the dynamics of three-dimensional axisymmetric vesicles in Navier-Stokes flows*, J. Comput. Phys., 257 (2014), pp. 670–686.

[25] C.-H. WU, T. G. FAI, P. J. ATZBERGER, AND C. S. PESKIN, *Simulation of osmotic swelling by the stochastic immersed boundary method*, SIAM J. Sci. Comput., 37 (2015), pp. B660–B688.

[26] Y. SEOL, W.-F. HU, Y. KIM, AND M.-C. LAI, *An immersed boundary method for simulating vesicle dynamics in three dimensions*, J. Comput. Phys., 322 (2016), pp. 125–141.

[27] W. HELFRICH, *Elastic properties of lipid bilayers: Theory and possible experiments*, Z. Naturforsch C, 28 (1973), pp. 693–703.

[28] X. LIU, F. SONG, AND C. XU, *An efficient spectral method for the inextensible immersed interface in incompressible flows*, Commun. Comput. Phys., 25 (2019), pp. 1071–1096.

[29] F. H. HARLOW AND J. E. WELSH, *Numerical calculation of time-dependent viscous incompressible flow of fluid with a free surface*, Phys. Fluids, 8 (1965), pp. 2181–2189.

[30] M.-C. LAI AND Y. SEOL, *A short note on Navier-Stokes flows with an incompressible interface and its approximations*, Appl. Math. Lett., 65 (2017), pp. 1–6.

[31] T. DAVIS, *An unsymmetric-pattern multifrontal method for sparse LU factorization*, SIAM J. Matrix Anal. Appl., 18 (1997), pp. 140–158.

[32] T. FUKUSHIMA, *Precise and fast computation of complete elliptic integrals by piecewise minimax rational function approximation*, J. Comput. Appl. Math., 282 (2015), pp. 71–76.

[33] J. P. BOYD, *Numerical, perturbative and Chebyshev inversion of the incomplete elliptic integral of the second kind*, Appl. Math. Comput., 218 (2012), pp. 7005–7013.

[34] T. FUKUSHIMA, *Precise and fast computation of a general incomplete elliptic integral of second kind by half and double argument transformations*, J. Comput. Appl. Math., 235 (2011), pp. 4140–4148.

[35] X. YANG, X. ZHANG, Z. LI, AND G.-W. HE, *A smoothing technique for discrete delta functions with application to immersed boundary method in moving boundary simulations*, J. Comput. Phys., 228 (2009), pp. 7821–7836.

[36] Y. LIU AND Y. MORI, *Properties of discrete delta functions and local convergence of the immersed boundary method*, SIAM J. Numer. Anal., 50 (2012), pp. 2986–3015.

[37] H. ZHOU AND C. POZRIKIDIS, *Deformation of liquid capsules with incompressible interfaces in simple shear flow*, J. Fluid Mech., 283 (1995), pp. 175–200.

[38] Z. LI AND M.-C. LAI, *New finite difference methods based on IIM for inextensible interfaces in incompressible flows*, East Asian J. Appl. Math., 1 (2011), pp. 155–171.

[39] W. HAGER, *Condition estimates*, SIAM J. Sci. Stat. Comput., 5 (1984), pp. 311–316.

[40] S. R. KELLER AND R. SKALAK, *Motion of a tank-treading ellipsoidal particle in a shear flow*, J. Fluid Mech., 120 (1982), pp. 27–47.

[41] M. KRAUS, W. WINTZ, U. SEIFERT, AND R. LIPOWSKY, *Fluid vesicles in shear flow*, Phys. Rev. Lett., 77 (1996), pp. 3685–3688.

[42] V. KANTSLER AND V. STEINBERG, *Orientation and dynamics of a vesicle in tank-treading motion in shear flow*, Phys. Rev. Lett., 95 (2005), 258101.

[43] S.K. VEERAPANENI, D. GUEYFFIER, D. ZORIN, AND G. BIROS, *A boundary integral method for simulating the dynamics of inextensible vesicles suspended in a viscous fluid in 2D*, J. Comput. Phys., 228 (2009), pp. 2334–2353.